

Article

The Physical Behavior of Protected Coal Seams Based on Triaxial Unloading Conditions

Zhiheng Chen *, Junhua Xue, Lanlan Guo, Renhui Cheng, Quanlin Yang and Jian Xiao

College of Safety Science and Engineering, Xi'an University of Science and Technology, Xi'an 710054, China; xuejunhua2003@163.com (J.X.); g18579782802@163.com (L.G.); crhalzj@126.com (R.C.); quanlinyang@xust.edu.cn (Q.Y.); xiaojian2025@163.com (J.X.)

* Correspondence: 22120089023@stu.xust.edu.cn

Abstract: Protective seam mining is the most economical and effective measure for eliminating coal and gas herniation. To study the unloading effect of the mining of a protective seam on the protected layer, and to better grasp the effect of the protective layer on the abatement, conventional triaxial tests were conducted on coal samples with the unloading of the axial pressure and the peripheral pressure. The results showed that, under the unloading path, the bias stress–axial strain curve showed a sudden upward trend upon unloading, and the slope of the curve increased suddenly, which was more obvious after the peripheral pressure exceeded 10 MPa; stress unloading before the peak accelerated the yielding of the specimen. Under the unloading test path, the deformation modulus of the coal samples decreased with the decrease in the perimeter pressure, while the damage factor and Poisson's ratio increased with the decrease in the perimeter pressure. Compared to the conventional triaxial test, under the unloading condition, the cohesion of the coal samples at peak stress decreased by 93.41% and the angle of internal friction increased by 37.41%, while the cohesion at the moment of residual strength decreased by 89.60% and the angle of internal friction increased by 37.44°. The brittleness index of the coal samples under unloading conditions with a peripheral pressure of 5 MPa, 10 MPa, 15 MPa, and 20 MPa increased by 178.83%, 159.18%, 87.93%, and 63.89%, respectively, compared to the conventional triaxial test. It can be seen that the greater the enclosing pressure, the smaller the difference in the brittleness index of the coal body.

Keywords: coal seam group; protective seam; stress; deformation modulus; Poisson's ratio



Citation: Chen, Z.; Xue, J.; Guo, L.; Cheng, R.; Yang, Q.; Xiao, J. The Physical Behavior of Protected Coal Seams Based on Triaxial Unloading Conditions. *Sustainability* **2024**, *16*, 922. <https://doi.org/10.3390/su16020922>

Academic Editor: Andrea Nicolini

Received: 29 September 2023

Revised: 29 December 2023

Accepted: 9 January 2024

Published: 22 January 2024



Copyright: © 2024 by the authors. Licensee MDPI, Basel, Switzerland. This article is an open access article distributed under the terms and conditions of the Creative Commons Attribution (CC BY) license (<https://creativecommons.org/licenses/by/4.0/>).

1. Introduction

During mining, disasters such as gas, sudden water, ground pressure, and dust pose serious threats to workers' lives and health [1–5], and with the mining of shallow coal resources, coal resources must be worked at greater depths [6]. Under deep mining conditions, the coal seam itself, the stress distribution thereon, and the gas assignment characteristics tend to be complicated, and the form of the coal seam group assignment becomes more common [7]. Under prevailing mining conditions in coal seam groups, the mining of the protective seam destroys the stress balance in the underlying coal and rock body, and with the advance of the protective seam mining surface, stress concentration develops in front of the coal wall, while the supporting pressure propagates along the bottom coal and rock seam, which in turn affects the lower coal seam, concentrating the stress in the affected coal seam. As the protective seam continues to advance, the stress above decreases and the protected seam is decompressed [8–11]. Therefore, under the influence of the protective seam mining effect, the lower protected seam undergoes a dynamic loading process involving a stress increase and decrease. Based on this, it is necessary to conduct experimental research into the unloading of the protective seam coal body under such conditions.

Protective seam mining can realize both the stress unloading of the coal body of the protected seam, which reduces the possibility of high-energy disasters, and the resolution

of the original adsorbed state gas in the coal body of the protected seam [12], which provides conditions for the extraction of gas from the protected seam. Gas threatens the safe production of coal mines [13–15], but it is also a clean energy source [16]. It is economical (and indeed sensible) to conduct coal seam mining while also achieving the extraction and utilization of unburdened gas [17]. Numerous scholars have studied the deformation and damage characteristics of the overlying and underlying coal rock layers during protective seam mining through numerical simulation and analyzed parameters such as the stress change characteristics and expansion and deformation rates of the protected layer. These studies provide practical reference values for coal and gas protrusion, gas extraction, and coal and gas co-mining [18–22]. At the same time, laboratory physical similarity simulation tests have also been widely used to study the mechanical properties and damage characteristics of the overlying coal seams during protective seam mining, which is also the most common approach adopted when providing reference values for practical engineering [23–25]. Compared to a single research approach, a combination of multiple approaches is more convincing and can better serve the actual project [26–28]. The unloading effect of protective seam mining on the protective seam is affected by many factors. Lei [29] studied the unloading and anti-scouring effects and the mechanism of the subducted coal rock under protective seam mining conditions, comparing the effects of the factors such as the height of protective seam mining, working face length, interval lithology, section coal pillar width, and layer spacing on the unloading effect of the lower protective coal seam. The results indicated that the layer spacing had the greatest effect. Cheng [30] studied the effect of soft rock protective seam mining on the pressure relief effect of the protected seam, and also concluded that the layer spacing had the largest effect. As the spacing between the protective seam layers changed, the burial depth of the coal seam also changed, and the mining of the protective seam exerted some influences on the stress path to which the protective layer was subjected. Based on this, scholars simplified the effect of protective seam mining on the stress path of the protective seam. To achieve this purpose, they explored test paths, such as unloading the circumferential pressure while increasing the axial pressure [31], stabilizing the circumferential pressure to unload the axial pressure [32], and cyclic loading and unloading [33]. These studies provide a theoretical basis for understanding the mechanical deformation and permeability characteristics of the coal body of the protective seam under protective seam mining conditions. Ground stress is the main factor that restricts the development and utilization of underground resources, so it is necessary to study the mechanical effects of underground rock masses [34–37], and it is even more necessary to study the unloading mechanism.

Based on the above research, we investigated the changes in the stress in the protective seam caused by the change in the support pressure in front of the coal wall during the protective seam mining process. Additionally, we simplified the stress path in the protective seam to obtain the loading and unloading scheme of the unloading test. On this basis, laboratory triaxial unloading test research was conducted to provide a reference for the unloading characteristics of the coal body in the protective seam under protective seam mining conditions.

2. Experimental Process

2.1. Theoretical Solution of Stress Distribution in the Bottom Plate of the Protective Layer Mining

Coal seams with a tendency for outbursts require that coal and gas outbursts are eliminated before mining [38], and mining to protect the layer has a good effect on eliminating outbursts. Cheng [39] simplified the stress boundary condition model of the bottom plate model by treating the bottom plate stress field problem as a semi-infinite plane strain problem subjected to a non-uniform load $q(x)$, as shown in Figure 1.

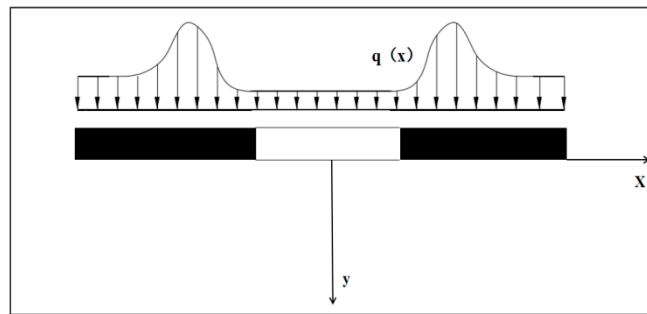


Figure 1. Model of the force on the floor.

Using the stress function method to solve for the mining stress field in the bottom plate, the stress function is written as follows.

$$U = U(x, y) \quad (1)$$

The boundary conditions of this mechanical analysis model can be found from the model simplification.

$$\left(\begin{array}{l} (\sigma_y)_{y=0} = \left(\frac{\partial^2 U}{\partial x^2} \right)_{y=0} = -q(x) \\ (\tau_{xy})_{y=0} = \left(\frac{\partial^2 U}{\partial x \partial y} \right)_{y=0} = 0 \end{array} \right) \quad (2)$$

The Fourier transform of the second and fourth order derivative functions of the stress function can be expressed as follows.

$$\left(\begin{array}{l} F[U''(x, y)] - \lambda^2 F[U(x, y)] \\ F[U^{(4)}(x, y)] = -\lambda^4 F[U(x, y)] \end{array} \right) \quad (3)$$

From the knowledge of elastic mechanics, the bi-tunable sum equation of the stress solution of the plane problem can be written as follows.

$$\left(\frac{\partial^2 U}{\partial x^2} + \frac{\partial^2 U}{\partial y^2} \right) \left(\frac{\partial^2 U}{\partial x^2} + \frac{\partial^2 U}{\partial y^2} \right) = 0 \quad (4)$$

The Fourier transform of the double reconciliation in Equation (4) and the stress boundary condition in Equation (2) along the x-direction shows that Equations (2) and (4) can be expressed by Equations (5) and (6), respectively.

$$\frac{d^4 u}{dy^4} - 2\lambda \frac{d^2 u}{dy^2} + \lambda^4 u = 0 \quad (5)$$

$$\left(\begin{array}{l} -\lambda^2 (u)_{y=0} = -z(\lambda) \\ \lambda \left(\frac{du}{dy} \right)_{y=0} = 0 \end{array} \right) \quad (6)$$

According to the theory of the Fourier transform, the unknown functions u , z in Equation (6) can be expressed by Equation (7).

$$\left(\begin{array}{l} u(x, y) = \frac{1}{\sqrt{2\pi}} \int_{-\infty}^{\infty} U(x, y) e^{i\lambda x} dx \\ z(\lambda) = \frac{1}{\sqrt{2\pi}} \int_{-\infty}^{\infty} q(x) e^{i\lambda x} dx \end{array} \right) \quad (7)$$

Solving the differential in Equation (5) yields the exponential form of the general solution of this differential equation.

$$u(\lambda, y) = Ae^{\lambda y} + Be^{-\lambda y} + C\lambda y e^{\lambda y} + D\lambda y e^{-\lambda y} \quad (8)$$

To ensure that the solution is bounded when y tends toward infinity, i.e., the coal seam is buried at a large depth, the following condition must be met: $A = C = 0$. Taking the absolute values in Equation (8), Equation (8) can be transformed into the following.

$$u = [B + D|\lambda|y]e^{-|\lambda|y} \quad (9)$$

Substituting the boundary condition Equation (6) into Equation (9) yields the unknown constant in the following equation.

$$B = D = \frac{z(\lambda)}{\lambda^2} \quad (10)$$

Substituting the unknown constant analytic Equation (10) into Equation (9) yields the following.

$$u = \frac{z(\lambda)}{\lambda^2}(1 + |\lambda|y)e^{-|\lambda|y} \quad (11)$$

The transformation stress corresponding to Equation (11) can be written as follows.

$$\left(\begin{array}{l} F(\sigma_x) = \frac{d^2u}{dy^2} = -z(\lambda)[1 - |\lambda|y]e^{-|\lambda|y} \\ F(\sigma_y) = -\lambda^2u = -z(\lambda)[1 + |\lambda|y]e^{-|\lambda|y} \\ F(\tau_{xy}) = i\lambda \frac{du}{dy} = -z(\lambda)[i|\lambda|y]e^{-|\lambda|y} \end{array} \right) \quad (12)$$

To determine its inverse transformation, the inverse function of each function in the right-hand side of Equation (11) can be expressed by Equation (13).

$$\left(\begin{array}{l} F^{-1}\left[(1 - |\lambda|y)e^{-|\lambda|y}\right] = 2^{3/2}\pi^{-1/2}x^2y(x^2 + y^2)^{-2} \\ F^{-1}\left[(1 + |\lambda|y)e^{-|\lambda|y}\right] = 2^{3/2}\pi^{-1/2}x^2y^3(x^2 + y^2)^{-2} \\ F^{-1}\left[i|\lambda|ye^{-|\lambda|y}\right] = 2^{3/2}\pi^{-1/2}x^2y^2(x^2 + y^2)^{-2} \end{array} \right) \quad (13)$$

According to the convolution theorem, if these functions are the Fourier transforms of the functions, then Equation (14) can be written as follows.

$$\int_{-\infty}^{\infty} F(\lambda)G(\lambda)e^{-i\lambda x}d\lambda = \int_{-\infty}^{\infty} f(\zeta)g(x - \zeta)d\zeta \quad (14)$$

Using Equation (12) and the convolution theorem from Equation (13), the analytical solution of the stress distribution in the bottom plate subjected to a non-uniform load semi-infinite body can be obtained, that is, the protective seam after mining, as follows.

$$\left(\begin{array}{l} \sigma_x = -\frac{2y}{\pi} \int_{-\infty}^{\infty} \frac{(x-\zeta)^2 q(\zeta)}{[(x-\zeta)^2 + y^2]^2} d\zeta \\ \sigma_y = -\frac{2y^3}{\pi} \int_{-\infty}^{\infty} \frac{q(\zeta)}{[(x-\zeta)^2 + y^2]^2} d\zeta \\ \tau_{xy} = -\frac{2y^2}{\pi} \int_{-\infty}^{\infty} \frac{(x-\zeta)q(\zeta)}{[(x-\zeta)^2 + y^2]^2} d\zeta \end{array} \right) \quad (15)$$

Since the self-weight of the subgrade rock was not considered after simplifying the bottom into a semi-infinite plane body, the stress distribution in the actual bottom should be based on Equation (15), plus the stress level due to the self-weight of the bottom rock layer.

$$\left(\begin{array}{l} \sigma_x = -\frac{2y}{\pi} \int_{-\infty}^{\infty} \frac{(x-\zeta)^2 q(\zeta)}{[(x-\zeta)^2 + y^2]^2} d\zeta - \gamma y \\ \sigma_y = -\frac{2y^3}{\pi} \int_{-\infty}^{\infty} \frac{q(\zeta)}{[(x-\zeta)^2 + y^2]^2} d\zeta - \kappa \gamma y \\ \tau_{xy} = -\frac{2y^2}{\pi} \int_{-\infty}^{\infty} \frac{(x-\zeta)q(\zeta)}{[(x-\zeta)^2 + y^2]^2} d\zeta \end{array} \right) \quad (16)$$

2.2. Coal Sample Preparation

The coal samples used for the test were taken from a mine in Henan Province, China. The burial depth of this coal seam was about 800 m. Assuming a vertical stress gradient of 25 kPa/m, the geostress was 20 MPa. When drilling for coal blocks down the mine, care was taken that the sampling locations were not too far away to avoid excessive differences between the coal samples. When selecting the target briquettes, the smaller and more broken briquettes were eliminated, and the selected briquettes were transported to the surface, sealed and impact-proofed, and then transported to the laboratory for processing. The prepared coal specimens are shown in Figure 2.



Figure 2. Partial coal specimens.

2.3. Test Scheme and Test Process

2.3.1. Test Scheme

In the form of a coal seam group assignment, during protective seam mining, a stress concentration develops in front of the coal wall, and the support pressure propagates downward along the bottom plate of the protective seam. This can disrupt the original stress state of the lower protective seam, resulting in stress on the coal seam within the zone of influence exceeding its original value, thus causing the stress concentration in the lower protected coal seam. The stress concentration in the protected seam was weaker than that in the protective seam because of the loss in the process of the stress transfer. As the working face of the protective layer advanced, the degree of stress concentration gradually decreased, and the disturbed coal seam underneath unloaded and expanded. With the collapse and compaction of the protective seam mining hollow area, the stress under the protected layer gradually recovered.

According to the stress state experienced successively by the protected layer under the protective seam mining for the simplified design of the test chamber stress path, the stress path of the unloading penetration test was obtained in three stages, namely the preloading stage, the axial compression stage, and the simultaneous unloading of the axial pressure and the surrounding pressure.

2.3.2. Test Process

The equipment used for the experiment is shown in Figure 3.

Conventional triaxial tests: Conventional triaxial compression tests were conducted under four hydrostatic pressure conditions of 5 MPa, 10 MPa, 15 MPa, and 20 MPa. In the preloading stage, the axial and radial stresses were applied to the set value by means of equal pressure loading, and the loading rate was 1 MPa/min. In the stabilization phase, the hydrostatic pressure state was maintained for a certain period of time. In the loading phase, a constant circumferential pressure was applied under a displacement control (0.2 mm/min)

as well as an axial pressure until the end of the test (deemed to be the time when the sample was damaged).



Figure 3. Experimental equipment.

Unloading tests: In the preloading stage, axial and radial stresses were applied to the set value by means of equal pressure loading. In the stabilization phase, the hydrostatic pressure state was maintained for a certain period of time. In the loading phase, constant circumferential pressure was applied at a rate of 0.002 mm/s to a predetermined stress (0.8 times the triaxial compressive strength).

In the unloading stage, an axial displacement control and a circumferential stress control were adopted to ensure that the axial stress could continue to be applied beyond the peak. The circumferential and axial pressures were reduced unequally, and the rate of circumferential pressure reduction was greater than that of axial pressure reduction, where the axial loading rate was reduced to 0.001 mm/s and the rate of circumferential pressure reduction was 0.1 MPa/s. Immediately after the destruction of the coal sample during the test, we stopped unloading the surrounding pressure, and continued to load the axial pressure in the original manner until the end of the test.

3. Experimental Results

Under conventional triaxial compression test conditions, the internal fracture development characteristics of the coal samples at different stress stages were different, and the internal fracture evolution of the coal samples changed irreversibly when the stress reached the yield stress. The coal samples were destroyed when the peak stress was reached, while the destroyed coal samples still bore a certain residual stress under the action of the surrounding pressure. According to the results of the conventional triaxial compression tests, it can be concluded that when the stress reached 0.8 times the peak stress, the coal sample was in the plastic deformation stage. Therefore, during the unloading test, 0.8 times the peak stress was selected as the unloading point.

According to the stress–strain results of the coal body under the conventional triaxial test conditions, the unloading starting point of the unloading path was selected, and unequal unloading perimeter pressure and axial pressure tests were conducted. The stress–strain curves are shown in Figure 4.

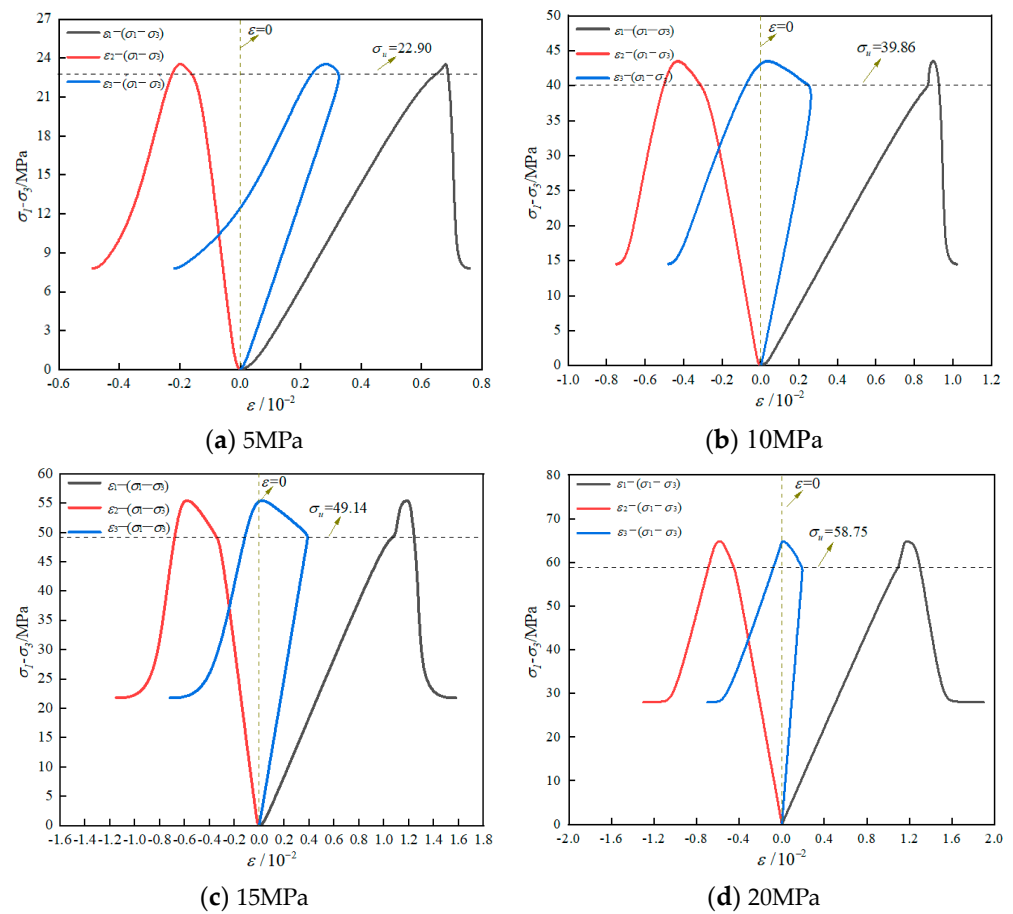


Figure 4. Stress–strain curves of coal under the unloading path.

Figure 4 shows that the stress path experienced by the coal sample before unloading was consistent with that under conventional triaxial test conditions, and its stress–strain curve was similar to that of the conventional triaxial test. However, upon axial and radial unloading, the stress–axial strain curve demonstrated a sudden upwards trend. The slope of the curve suddenly increased, the yielding stage before the peak was significantly shorter than that of the conventional triaxial test, and the axial strain value at the maximum partial stress decreased significantly, i.e., the unloading path before the peak accelerated the yielding of the specimen. From the unloading point, the bias stress–lateral strain curve trended downwards, the slope of the curve decreased, and the bias stress–volume strain curve suddenly changed its original trend after the start of unloading and appeared to turn left, indicating that the deformation of the coal sample changed from compressive to expansive. According to the post-peak curve, it can be seen that the post-peak stress drop gradient of the unloaded coal body under the four circumferential pressures was larger, i.e., the axial strain changed less during the post-peak stress drop, indicating that the post-peak damage of the unloaded coal sample was dominated by brittle damage characteristics, and its ductile damage characteristics were substantially weakened compared to those observed during conventional triaxial testing.

4. Discussion

4.1. Analysis of the Deformation Parameter Variation Characteristics

The formula for calculating the deformation parameters of the material under uniaxial compression test conditions is shown below.

$$E = \frac{\sigma_1}{\varepsilon_1} \quad (17)$$

$$\mu = -\frac{\varepsilon_3}{\varepsilon_1} \quad (18)$$

where E is the modulus of elasticity and μ is the Poisson's ratio.

Under conventional triaxial test conditions, the surrounding pressure was unchanged, and in Equation (17) could be replaced by $\sigma_1 - \sigma_3$ and thus calculate the deformation parameters. Under the unloading path, the surrounding pressure started to decrease from the unloading point, so the solution of the deformation parameters was also different from the conventional triaxial solution method, requiring consideration of the effects of lateral deformation and the surrounding pressure. According to the previous research [40–42], a generalized form of Hooke's law was invoked.

$$\begin{cases} E = \frac{\sigma_1 - 2\mu\sigma_3}{\varepsilon_1} \\ \mu = \frac{B\sigma_1 - \sigma_3}{\sigma_3(2B-1) - \sigma_1} \\ B = \frac{\varepsilon_3}{\varepsilon_1} \end{cases} \quad (19)$$

4.2. Deformation Modulus Analysis

The calculation was carried out according to Equation (19), and the variation curve of the deformation modulus of the coal samples with the surrounding pressure during unloading was plotted, as shown in Figure 5.

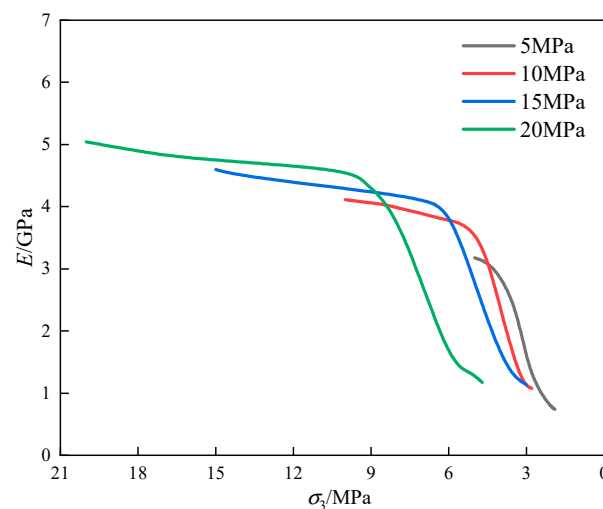


Figure 5. Deformation modulus of the coal samples under the unloading path.

As illustrated in Figure 5, the deformation modulus decreased with the unloading of the surrounding pressure, and its decrease was divided into two stages, with a gentle decreasing trend in the first stage and a sharp decrease in the second stage. Under different initial envelope pressures, the deformation modulus also showed an increasing trend with an increase in the initial envelope pressure at the beginning of the unloading stage. With continued unloading, the curves showed a change in the deformation modulus with an envelope pressure cross, showing certain dispersion and uncertainty.

4.3. Analysis of the Deterioration of the Deformation Modulus

As shown in Figure 5, the deformation modulus showed a clear deterioration effect with the decrease in the surrounding pressure. To clarify the evolution of damage to the coal samples during unloading, the damage caused by unloading was assumed to be uniformly distributed within the coal sample, and the one-dimensional damage factor [43]

was defined according to the effective stress concept and strain equivalence principle, as shown below.

$$D = 1 - \frac{\tilde{E}}{E_0} \tag{20}$$

where \tilde{E} is the effective deformation modulus during unloading and E_0 is the deformation modulus at the initial point of unloading.

Based on Equation (20), the variation of the damage factor with the surrounding pressure was obtained, as shown in Figure 6.

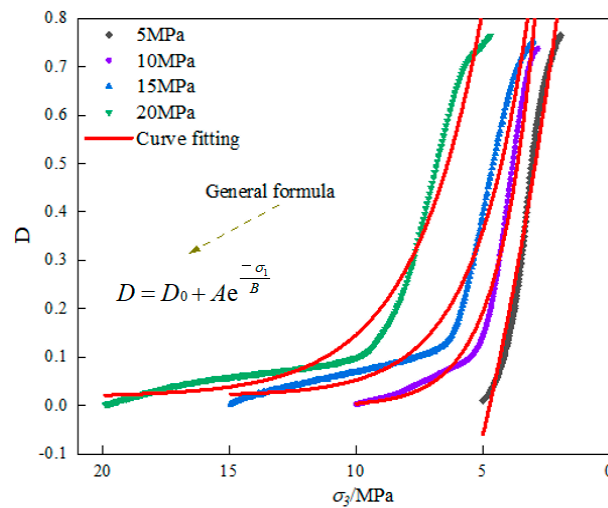


Figure 6. Deterioration characteristics of the damage factor of the coal samples under the unloading path.

According to the trend in the deterioration of the deformation modulus of the coal body after the start of unloading, the damage factor pertaining to the coal body increased with the decrease in the surrounding pressure (the trend was flat at first, then rapid). At the same time, the damage factor increased with the increase in the initial surrounding pressure. The relationship between the damage factor and the surrounding pressure in the figure was fitted, and the fitting general formula, fitting parameters, and their correlation coefficients for the coal damage factor and the surrounding pressure under different initial surrounding pressures are shown in Table 1. As shown in Figure 6, the regression curve fit the test data. Three of the fitting parameters could be expressed as polynomial functions of the initial envelope pressure, as shown in Equation (21).

$$\begin{cases} A = 0.0127\sigma_3^3 - 0.49195\sigma_3^2 + 5.76233\sigma_3 - 15.06026 \\ B = 0.04745\sigma_3^2 - 1.34511\sigma_3 + 10.89527 \\ D_0 = 0.00168\sigma_3^3 - 0.07586\sigma_3^2 + 1.10523\sigma_3 - 5.14394 \end{cases} \tag{21}$$

Table 1. Damage parameter fitting curve and the related parameters.

Fitting Equation	Initial Confining Pressure/MPa	A	B	D ₀	R ²
$D = D_0 + Ae^{\frac{-\sigma_3}{B}}$	5	3.07038	5.60142	−1.31807	0.97580
	10	6.12552	1.45330	−0.00254	0.97893
	15	3.57130	2.13161	0.01971	0.97187
	20	5.02598	2.72875	0.01770	0.96784

4.4. Analysis of Poisson’s Ratio Variation Characteristics

According to Equation (20), the variation of Poisson’s ratio with the surrounding pressure was obtained, as shown in Figure 7.

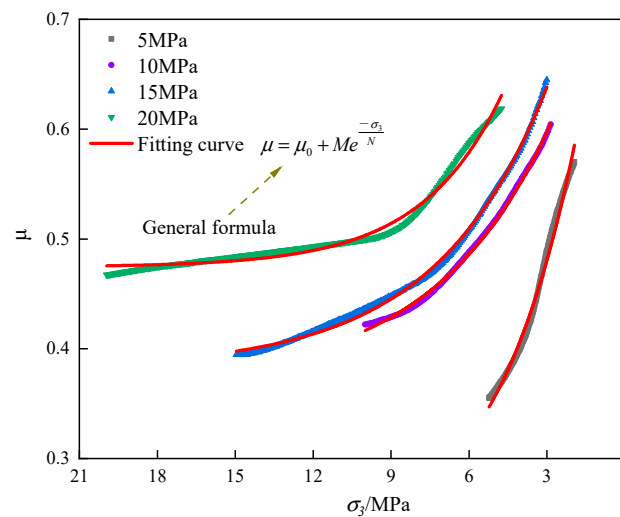


Figure 7. Deterioration characteristics of the poisson’s ratio of the coal samples under the un-loading path.

As presented in Figure 7, during the unloading process, Poisson’s ratio decreased with the decrease in the surrounding pressure, slowly increasing in the first period and sharply increasing thereafter. Meanwhile, the generalized Poisson’s ratio exceeded 0.5. According to the analysis of the stress state of the coal body and its deformation characteristics during the test, it was known that the unloading of circumferential pressure could be equivalent to applying tensile stress in the ring direction of the coal sample. The lateral deformation of the coal body developed rapidly under the action of ring stress, causing Poisson’s ratio to exceed the limiting value. Poisson’s ratio tended to increase with the increase in the initial surrounding pressure.

The relationship between Poisson’s ratio and the surrounding pressure was fitted by using the general equation of exponential function, and the relationship between Poisson’s ratio and the surrounding pressure of the coal samples under different initial surrounding pressure was obtained. The fitting equation and the fitting parameters are listed in Table 2.

Table 2. Poisson’s ratio fitting curve and the related parameters.

Fitting Equation	Initial Confining Pressure/MPa	M	N	μ ₀	R ²
$\mu = \mu_0 + Me^{-\frac{\sigma_3}{N}}$	5	0.68169	3.18992	0.21442	0.9913
	10	0.44648	4.52193	0.36765	0.9984
	15	0.51624	4.28636	0.38208	0.9979
	20	0.72289	3.10297	0.47438	0.9853

M and N are the coefficients related to the nature of the coal body itself and the stress paths and magnitudes of the applied stresses. μ₀ can be used to characterize the ratio of lateral deformation to axial deformation in the more stable unloading phase before the peak of the coal sample. As shown in Figure 7, the regression curves fit the test data. Three of the fitted parameters could be expressed as polynomial functions of the initial enclosing pressure, as given by the following.

$$\begin{cases} M = 0.00442\sigma_3^2 - 0.1066\sigma_3 + 1.09581 \\ N = -0.02515\sigma_3^2 + 0.61892\sigma_3 + 0.75515 \\ \mu_0 = 0.00029\sigma_3^3 - 0.01133\sigma_3^2 + 0.15021\sigma_3 - 0.29134 \end{cases} \quad (22)$$

4.5. Analysis of the Strength Characteristics of Coal on the Unloading Path

According to the stress–strain curves obtained from the conventional triaxial and unloading tests, the peak strength of the unloaded coal sample was lower than that of the

conventional triaxial at the same initial enclosing pressure. According to the relationship between the change in the axial stress and circumferential stress of the coal samples during the unloading test, the peak strength and residual strength curves of the unloaded coal samples under different circumferential pressures were plotted and compared with the conventional triaxial. The relationship curves were fitted using linear functions, as shown in Figure 8.

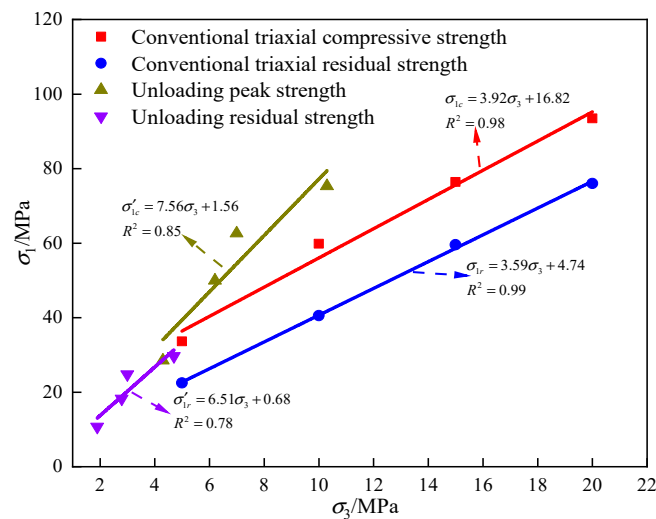


Figure 8. Strength characteristics of coal in the conventional triaxial test and unloading test.

The Mohr–Coulomb intensity criterion is shown in Equation (23).

$$\sigma_1 = \frac{1 + \sin \phi}{1 - \sin \phi} \sigma_3 + \frac{2c \cdot \cos \phi}{1 - \sin \phi} \quad (23)$$

The general equation obtained by fitting the experimental data is shown in Equation (24).

$$\sigma_1 = a\sigma_3 + b \quad (24)$$

Namely,

$$a = \frac{1 + \sin \phi}{1 - \sin \phi} \quad (25)$$

$$b = \frac{2c \cdot \cos \phi}{1 - \sin \phi} \quad (26)$$

where a and b are the fitting parameters, c is the cohesion, and ϕ is the angle of internal friction.

The cohesion and the angle of internal friction were solved according to the fitted relationship and parameters pertaining to the data shown in Figure 8. The cohesion of the peak of the conventional triaxial test was calculated to be 4.25 MPa, the cohesion of the residual strength was 1.25 MPa, the cohesion of the peak of the unloading test was 0.28 MPa, and the cohesion of the residual strength was 0.13 MPa. The internal friction angle of the peak of the conventional triaxial test was 36.41° , the internal friction angle of the residual strength was 34.35° , the internal friction angle of the peak of the unloading test was 50.03° , and the internal friction angle of the residual strength was 47.17° . The internal friction angle of the peak of the unloading test was 50.03° , and the internal friction angle of the residual strength was 47.17° . It can be seen that the cohesion of the coal body under unloading conditions was significantly reduced, while the angle of internal friction increased. The cohesion of the coal samples under unloading conditions was found to be significantly reduced, which was because the binding force of microcracks was weakened during the unloading test due to the reduction in the surrounding pressure, allowing the coal body

expand more. The surrounding pressure remained unchanged during conventional triaxial testing, so there was a clear difference between the two. Meanwhile, the cohesion of the residual strength was reduced by 70.59% from the peak in the conventional triaxial test and by 53.57% in the unloading test. There was a 5.66% reduction in the internal friction angle of the residual strength from the peak in the conventional triaxial test and a 5.72% reduction in the unloading test. It was shown that the cohesion decreased more, while the internal friction angle decreased less and the change therein was insignificant.

4.6. Analysis of the Brittleness and Ductility Transformation of the Coal Samples

Based on the previous studies, it is known that the mechanical response of the coal rock body exhibits significant pressure correlation [44], and based on the present research results, the characteristic stresses (yield stress, peak stress, and residual stress) on the coal body all increased with the increase in the envelope pressure. The analysis of Figures 4 and 5 revealed that the extent of the pressure drop after the peak of the stress–strain curve of the coal sample varied with the increase in the surrounding pressure, i.e., the damage characteristics of the coal samples varied with the change in the surrounding pressure. The transformation process of the brittle and ductile properties of the coal rock mass under triaxial compression was generalized [45], as shown in Figure 9.

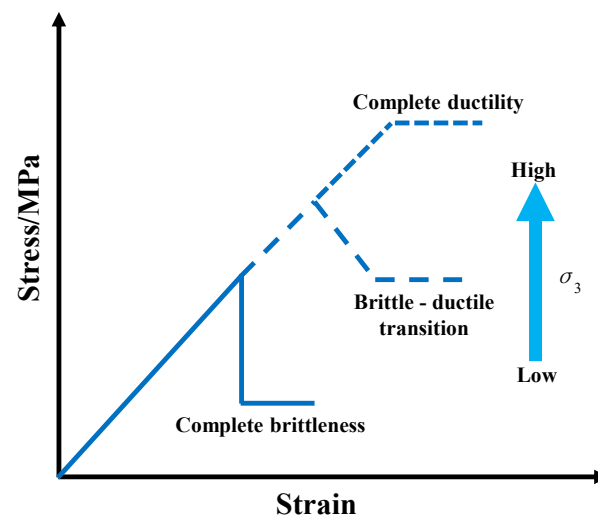


Figure 9. Schematic diagram of the transformation of the brittle–ductile characteristics of the samples.

Figure 9 demonstrated that when the surrounding pressure was low, the restraint capacity of lateral deformation of coal sample decreased, which made the post-peak stress fall rapidly and approach complete brittleness. With an increase in the surrounding pressure, the restraint capacity of lateral deformation increased continuously, the characteristic value of each stress of the coal sample increased continuously, the post-peak stress drop decreased continuously, and the transformation from brittle to ductile continued. When the surrounding pressure increased to a certain degree, the lateral deformation was significantly restrained. Even if the rock was damaged, its bearing capacity could still be maintained, i.e., a fully ductile state was mobilized.

Numerous scholars have conducted extensive research into the brittle nature of rock, and several rock brittleness indicators have been proposed based on rock strength indicators, stress–strain curves, and rupture angles. Zhang et al. [46] proposed a new brittleness index for studying rocks by considering the joint influence of the pre- and post-curve peaks on the degree of rock brittleness, as shown in Equation (27). Based on this, the

brittleness–ductility characteristics of the conventional triaxial tests and unloaded coal bodies were analyzed, as shown in Figure 10.

$$B_1 = \frac{\varepsilon_r(\sigma_{3c} - \sigma_r)}{\sigma_{3c}(\varepsilon_r - \varepsilon_{3c})} + \frac{2}{\pi\varepsilon_{3c}} \arctan \frac{\sigma_{3c}}{\varepsilon_{3c}} \quad (27)$$

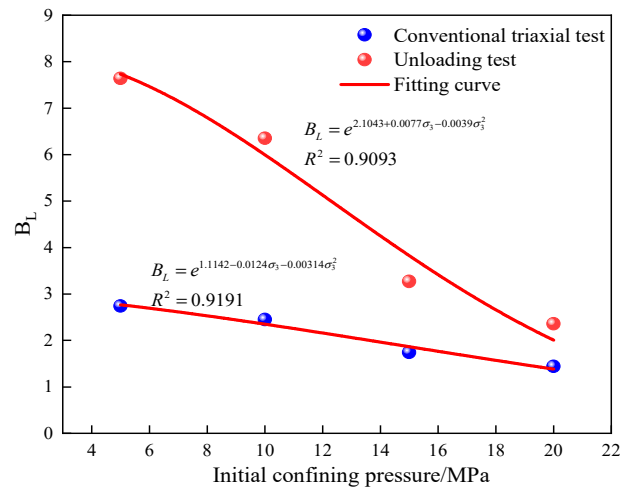


Figure 10. Change trend of the coal sample brittleness index.

As shown in Figure 10, the brittleness indices of the coal samples under conventional triaxial test conditions were all smaller than those in the unloading tests. The smaller the initial enclosure pressure, the greater the difference between the brittleness indices of the coal samples of the two test schemes. The larger the initial enclosure pressure, the smaller the difference, indicating that the brittleness of the coal samples under the unloading path was enhanced. This became more obvious when the initial enclosure pressure was lower. While under the same test path, the brittleness indices of the coal samples also decreased with the decrease in the enclosure pressure, and the range of the brittleness indices of the coal samples with the decrease in the enclosure pressure under the conventional triaxial test path was smaller than that under the unloading test path. This was because under the unloading path, with the reduction in the circumferential pressure, the circumferential binding force of the coal sample gradually weakened, especially when the initial circumferential pressure was small. The unloading of the circumferential pressure reduced the residual circumferential pressure to a lower level, which could not restrain the lateral deformation, leading to the destruction of the coal sample after making the post-peak stress fall sharply and making the brittle damage characteristics more obvious.

5. Conclusions

- (i) Under the unloading path, the bias stress–axial strain curve showed a sudden upward trend after the beginning of unloading, and the slope of the curve increased suddenly, which was more obvious after the peripheral pressure exceeded 10 MPa, and the stress unloading before the peak accelerated the yielding of the specimen.
- (ii) Under the unloading test path, the deformation modulus of the coal samples decreased with decreasing enclosure pressure, while the damage factor and Poisson's ratio increased with decreasing enclosure pressure.
- (iii) Compared to the conventional triaxial test, the cohesion at peak stress decreased by 93.41% and the angle of internal friction increased by 37.41% for the coal samples under unloading conditions. The residual cohesion decreased by 89.60% and the angle of internal friction increased by 37.44°.
- (iv) Compared to conventional triaxial test conditions, the brittleness indices of the coal samples under unloading conditions with an enclosing pressure of 5 MPa, 10 MPa, 15 MPa, and 20 MPa increased by 178.83%, 159.18%, 87.93%, and 63.89%, respectively.

The results indicated that the larger the circumferential pressure, the smaller the difference in the brittleness index.

Author Contributions: Methodology, Z.C.; Software, J.X. (Junhua Xue); Investigation, R.C.; Data curation, Z.C. and J.X. (Jian Xiao); Writing—original draft, Z.C.; Writing—review & editing, L.G. and Q.Y.; Funding acquisition, J.X. (Junhua Xue). All authors have read and agreed to the published version of the manuscript.

Funding: This study was funded by a grant from the National Natural Science Foundation of China (Grant number: 51974239).

Institutional Review Board Statement: Not applicable.

Informed Consent Statement: Not applicable.

Data Availability Statement: Data are contained within the article.

Conflicts of Interest: The authors declare no conflicts of interest.

References

- Lin, H.; Ji, P.; Kong, X.; Li, S.; Long, H.; Xiao, T.; Li, B. Experimental study on the influence of gas pressure on CH₄ adsorption-desorption-seepage and deformation characteristics of coal in the whole process under triaxial stress. *Fuel* **2023**, *333*, 126513. [[CrossRef](#)]
- Zhang, C.; Wang, P.; Wang, E.; Chen, D.; Li, C. Characteristics of coal resources in China and statistical analysis and preventive measures for coal mine accidents. *Int. J. Coal Sci. Technol.* **2023**, *10*, 22. [[CrossRef](#)]
- Liang, Y.; Yang, Y.; Guo, S.; Tian, F.; Wang, S. Combustion mechanism and control approaches of underground coal fires: A review. *Int. J. Coal Sci. Technol.* **2023**, *10*, 24. [[CrossRef](#)]
- Han, H.; Wang, H.; Zhang, Q.; Du, Y.; Wang, H.; Wang, H. Investigations of the effects of two typical jet crushing methods on the atomization and dust reduction performance of nozzles. *Int. J. Coal Sci. Technol.* **2023**, *10*, 50. [[CrossRef](#)]
- Wang, K.; Zhang, G.; Wang, Y.; Zhang, X.; Li, K.; Guo, W.; Du, F. A numerical investigation of hydraulic fracturing on coal seam permeability based on PFC-COMSOL coupling method. *Int. J. Coal Sci. Technol.* **2022**, *9*, 10. [[CrossRef](#)]
- Ranjith, P.; Zhao, J.; Ju, M.; De Silva, R.; Rathnaweera, T.; Bandara, A. Opportunities and Challenges in Deep Mining: A Brief Review. *Engineering* **2017**, *3*, 546–551. [[CrossRef](#)]
- Cheng, Z.; Qi, Q.; Li, H.; Zhang, L.; Liu, X. Evolution of the superimposed mining induced stress-fissure field under extracting of close distance coal seam group. *J. China Coal Soc.* **2016**, *41*, 367–375.
- Xie, H.; Zhao, X.; Liu, J.; Zhang, R.; Xue, D. Influence of different mining layouts on the mechanical properties of coal. *Int. J. Min. Sci. Technol.* **2012**, *22*, 749–755. [[CrossRef](#)]
- Zhang, L.; Huang, M.; Li, M.; Lu, S.; Yuan, X.; Li, J. Experimental Study on Evolution of Fracture Network and Permeability Characteristics of Bituminous Coal Under Repeated Mining Effect. *Nat. Resour. Res.* **2022**, *31*, 463–486. [[CrossRef](#)]
- Zhang, C.; Zhang, L. Permeability Characteristics of Broken Coal and Rock Under Cyclic Loading and Unloading. *Nat. Resour. Res.* **2019**, *28*, 1055–1069. [[CrossRef](#)]
- Zhao, T.; Zhang, P.; Xiao, Y.; Guo, W.; Zhang, Y.; Zhang, X. Master crack types and typical acoustic emission characteristics during rock failure. *Int. J. Coal Sci. Technol.* **2023**, *10*, 2. [[CrossRef](#)]
- Du, X.; Xue, J.; Ma, Q.; Chen, Z.; Zhan, K. Energy evolution characteristics of coal–rock composite bodies based on unidirectional load. *Nat. Resour. Res.* **2022**, *31*, 1647–1663. [[CrossRef](#)]
- Zhou, J.; Lin, H.; Jin, H.; Li, S.; Yan, Z.; Huang, S. Cooperative prediction method of gas emission from mining face based on feature selection and machine learning. *Int. J. Coal Sci. Technol.* **2022**, *9*, 51. [[CrossRef](#)]
- Ullah, B.; Cheng, Y.; Wang, L.; Yang, W.; Jiskani, M.; Hu, B. Experimental analysis of pore structure and fractal characteristics of soft and hard coals with same coalification. *Int. J. Coal Sci. Technol.* **2022**, *9*, 58. [[CrossRef](#)]
- Ji, P.; Lin, H.; Kong, X.; Li, S.; Hu, B.; Wang, P.; He, D.; Yang, S. Pore structure of low-permeability coal and its deformation characteristics during the adsorption–desorption of CH₄/N₂. *Int. J. Coal Sci. Technol.* **2023**, *10*, 51. [[CrossRef](#)]
- Wang, C.; Wang, H.; Elsworth, D.; Cui, G.; Li, B.; Zhou, M.; Li, W.; Zhang, J. Revaluating coal permeability–gas pressure relation under various gas pressure differential conditions. *Int. J. Coal Sci. Technol.* **2023**, *10*, 55. [[CrossRef](#)]
- Zou, Q.; Zhan, J.; Wang, X.; Huang, Z. Influence of nanosized magnesia on the hydration of borehole-sealing cements prepared using different methods. *Int. J. Coal Sci. Technol.* **2023**, *10*, 66. [[CrossRef](#)]
- Hou, P.; Xue, Y.; Gao, F.; Wang, S.; Jiao, X.; Zhu, C. Numerical Evaluation on Stress and Permeability Evolution of Overlying Coal Seams for Gas Drainage and Gas Disaster Elimination in Protective Layer Mining. *Min. Metall. Explor.* **2022**, *39*, 1027–1043. [[CrossRef](#)]
- Ren, S.; Tao, Z.; He, M.; Li, M.; Sui, Q. Numerical simulation study on shear resistance of anchorage joints considering tensile–shear fracture criterion of 2G-NPR bolt. *Int. J. Coal Sci. Technol.* **2023**, *10*, 58. [[CrossRef](#)]

20. Yuan, Y.; Chen, Z.; Zhang, X.; Wang, Z. Intermediate coal pillar instability and permeability evolution in extremely thin protective seam by auger mining. *Arab. J. Geosci.* **2019**, *12*, 322. [[CrossRef](#)]
21. Yu, S.; Zhu, W.; Niu, L. Experimental and numerical evaluation on debonding of fully grouted rockbolt under pull-out loading. *Int. J. Coal Sci. Technol.* **2022**, *9*, 8. [[CrossRef](#)]
22. Jin, H.; Yang, Z. Study on Reasonable Layout of Upper Protective Layer for Prevention Rock Burst under Coal Seam Group with Close Quarters Conditions. *Shock. Vib.* **2021**, *2021*, 6139935. [[CrossRef](#)]
23. Ji, P.; Lin, H.; Kong, X.; Li, S.; Cai, Y.; Wang, R.; Tian, Y.; Zhao, T. Experimental study on enhanced coal seam gas extraction by uniform pressure/pulse pressure N₂ injection. *Fuel* **2023**, *351*, 128988. [[CrossRef](#)]
24. Deng, D.; Wang, H.; Xie, L.; Wang, Z.; Song, J. Experimental study on the interrelation of multiple mechanical parameters in overburden rock caving process during coal mining in longwall panel. *Int. J. Coal Sci. Technol.* **2023**, *10*, 47. [[CrossRef](#)]
25. Huo, B.; Fan, Z.; Lu, Y.; Duan, Z.; Jing, X.; Xie, Z. Similarity simulation study on permeability of protected coal seam volumetric strain during mining protective coal seam. *Coal Sci. Technol.* **2018**, *46*, 19–26.
26. Qin, S.; Lin, H.; Yang, S.; Wei, Z. A mathematical model for parameter setting in discrete element numerical simulation. *Int. J. Coal Sci. Technol.* **2023**, *10*, 87. [[CrossRef](#)]
27. Ma, D.; Duan, H.; Li, Q.; Wu, J.; Zhong, W.; Huang, Z. Water–rock two-phase flow model for water inrush and instability of fault rocks during mine tunnelling. *Int. J. Coal Sci. Technol.* **2023**, *10*, 77. [[CrossRef](#)]
28. Liu, X.; Chen, H.; Liu, B.; Wang, S.; Liu, Q.; Luo, Y.; Luo, J. Experimental and numerical investigation on failure characteristics and mechanism of coal with different water contents. *Int. J. Coal Sci. Technol.* **2023**, *10*, 49. [[CrossRef](#)]
29. Lei, W. Study on the effect and mechanism of rock burst prevention by pressure relief of underlying coal and rock in protective coal seam mining. *Xi'an Univ. Sci. Technol.* **2021**, 58–81.
30. Cheng, X. Mechanical effect and application of mining relief-pressure for soft rock protective layer mining in deep strong outburst coal seam. *Anhui Univ. Sci. Technol.* **2019**, 64–90.
31. Yin, G.; Li, M.; Wang, J.; Xu, J.; Li, W. Mechanical behavior and permeability evolution of gas infiltrated coals during protective layer mining. *Int. J. Rock. Mech. Min.* **2015**, *80*, 292–301. [[CrossRef](#)]
32. Ding, K.; Wang, L.; Wang, W.; Li, Z.; Jiang, C.; Ren, B.; Wang, S. Experimental Study on Gas Seepage Characteristics of Axially Unloaded Coal under Different Confining Pressures and Gas Pressures. *Processes* **2022**, *10*, 1055. [[CrossRef](#)]
33. Li, Q.; Liang, Y.; Zou, Q. Seepage and Damage Evolution Characteristics of Gas-Bearing Coal under Different Cyclic Loading-Unloading Stress Paths. *Processes* **2018**, *6*, 190. [[CrossRef](#)]
34. Cheng, W.; Cui, G.; Tan, Y.; Elsworth, D.; Wang, C.; Yang, C.; Chen, T.; Jiang, C. A multi-layer nanocased model to explain the U-shaped evolution of shale gas permeability at constant confining pressure. *Fuel* **2024**, *359*, 130478. [[CrossRef](#)]
35. Cui, G.; Tan, Y.; Chen, T.; Feng, X.; Elsworth, D.; Pan, Z.; Wang, C. Multidomain two-phase flow model to study the impacts of hydraulic fracturing on shale gas production. *Energy Fuels* **2020**, *34*, 4273–4288. [[CrossRef](#)]
36. Cui, G.; Feng, X.; Pan, Z.; Chen, T.; Liu, J.; Elsworth, D.; Tan, Y.; Wang, C. Impact of shale matrix mechanical interactions on gas transport during production. *J. Pet. Sci. Eng.* **2020**, *184*, 106524. [[CrossRef](#)]
37. Cui, G.; Liu, J.; Wei, M.; Shi, R.; Elsworth, D. Why shale permeability changes under variable effective stresses: New insights. *Fuel* **2018**, *213*, 55–71. [[CrossRef](#)]
38. Xu, L.; Fan, C.; Luo, M.; Li, S.; Han, J.; Fu, X.; Xiao, B. Elimination mechanism of coal and gas outburst based on geo-dynamic system with stress–damage–seepage interactions. *Int. J. Coal Sci. Technol.* **2023**, *10*, 74. [[CrossRef](#)]
39. Cheng, Z. *Study on Crack Evolution and Permeability Characteristic of Protective Coal Seam Mining in Close Coal Seams Group*; China University of Mining & Technology: Beijing, China, 2018.
40. Huang, R.; Huang, D. Experimental research on affection laws of unloading rates on mechanical properties of Jinping marble under high geostress. *Chin. J. Rock. Mech. Eng.* **2010**, *29*, 21–33.
41. Gao, C.; Xu, J.; He, P.; Liu, J. Study on mechanical properties of marble under loading and unloading conditions. *Chin. J. Rock. Mech. Eng.* **2005**, *24*, 456–460.
42. Zhu, Z.; Wei, L.; Li, J.; Meng, Q.; Sui, B.; Zhang, Z. Deformation evolution and dissipated energy characteristics of marble under pre-peak unloading conditions. *J. China Coal Soc.* **2020**, *45*, 181–190.
43. Liu, Q.; Liu, K.; Lu, X.; Zhu, J. Study of mechanical properties of raw coal under high stress with triaxial unloading. *Chin. J. Rock. Mech. Eng.* **2014**, *33*, 3429–3438.
44. Xie, H.; Gao, M.; Fu, C.; Lu, Y.; Yang, M.; Hu, J.; Yang, B.G. Mechanical behavior of brittle-ductile transition in rocks at different depths. *J. China Coal Soc.* **2021**, *46*, 701–715.
45. Zhang, C.; Yu, J.; Bai, Y.; Cao, W.; Zhang, S.; Guo, Z. Statistical damage constitutive model of rock brittle-ductile transition based on strength theory. *Chin. J. Rock. Mech. Eng.* **2023**, *42*, 1–10.
46. Zhang, C.; Bai, Y.; An, Y.; Wang, H.; Zeng, X. A new method for evaluating rock brittle characteristics based on full stress-strain curve. *J. Highw. Transp. Res. Dev.* **2021**, *38*, 63–72.

Disclaimer/Publisher’s Note: The statements, opinions and data contained in all publications are solely those of the individual author(s) and contributor(s) and not of MDPI and/or the editor(s). MDPI and/or the editor(s) disclaim responsibility for any injury to people or property resulting from any ideas, methods, instructions or products referred to in the content.